

JOURNAL OF THE AMERICAN CHEMICAL SOCIETY

Registered in U.S. Patent Office. © Copyright, 1978, by the American Chemical Society

VOLUME 100, NUMBER 24 NOVEMBER 22, 1978

Fused Organic Salts. 8. Properties of Molten Straight-Chain Isomers of Tetra-*n*-pentylammonium Salts

John E. Gordon* and G. N. SubbaRao

Contribution from the Department of Chemistry, Kent State University,
Kent, Ohio 44242. Received March 21, 1978

Abstract: A representative selection of the 64 straight-chain isomers of tetra-*n*-pentylammonium cation (Q^+) has been prepared. Twenty-seven halides, perchlorates, and tetraphenylborates of these cations make up a suite of salts in which the cation's shape and the asymmetry of placement of its charge vary widely. Temperatures, heats, and entropies of solid-solid transition and fusion were measured by hot-stage microscopy and differential scanning calorimetry. Phase diagrams for a number of salt-salt and salt-nonelectrolyte systems were studied by hot-stage microscopy, and the permissible limits of structure variation in Q^+ for observation of complete miscibility of two solid salts are reported. The effect of Q^+ structure on the critical solution temperatures of salt-nonelectrolyte systems are reported for two nonelectrolytes. The molar volume (V_m) and surface tension (σ) of 11 liquid salts were determined over a 30–40 °C temperature range near the freezing point. As the charge placement in Q^+ becomes progressively more asymmetric, the quantity $\sigma/V_m^{1/3}$, taken as a measure of the cohesive energy density, rises to a maximum and then falls abruptly. The rising portion of this curve is predicted by a simple electrostatic model. Possible origins of the descending portion are discussed. A prefreezing anomaly for liquid dimethyldioctylammonium perchlorate is characterized by sharp breaks in the temperature dependence of surface tension and viscosity some 30 and 40 °C above the freezing point. R_f values for chromatography of $Q^+ClO_4^-$ and $Q^+Ph_4B^-$ on thin silicic acid layers in three solvent systems are reported. The dominant retardation mechanism appears to be nonelectrostatic.

The simple $R_4N^+A^-$ salts have been productive tools in electrolyte-solution chemistry,^{1–10} fused-salt chemistry,^{11,12} and organic reactivity manipulation.^{13–15} Some important aspects of their chemistry remain to be developed, however. Detailed modeling of charge distribution, shielding, and interaction with solvent and counterion largely remain to be worked out.^{16–20} More simply, the radii of these ions are not accurately fixed. The most commonly used values are equivalent-sphere radii determined from molecular models.²¹ Both in the crystal²² and in ion pairs in solution²³ Br^- is known to approach *n*- Pr_4N^+ more closely than the equivalent-sphere radius would imply; it penetrates between the alkyl chains of Pr_4N^+ . There is evidence that organic ions bearing the charge on a peripheral atom display effective radii in their electrostatic interactions that are much closer to the van der Waals radii of the charge-bearing atom than to the mean radii of the organic ions as a whole.²⁴ Since the charge in R_4N^+ is neither peripheral nor perfectly buried, the effective electrostatic radius must depend upon what charged site or sites the ion is interacting with. Can useful effective electrostatic radii for R_4N^+ be determined? Most of the work done with R_4N^+ has used the simple symmetrical ions tetramethyl through tetrabutyl. Radii of any description are presently lacking for the less symmetrically substituted ions RR'_3N^+ , $R_2R'_2N^+$, etc. In these cases the equivalent-sphere radius is still more of a simplification.

A second area of unfinished business is the short-range structure of the molten $R_4N^+A^-$ salts, in which unusual

transport properties have been attributed to intermeshing of alkyl chains and resulting anion entrapment.²⁵ A third is the interaction mechanism by which added nonelectrolyte molecules sometimes monotonically reduce the conductance of molten $R_4N^+A^-$ throughout the ultraconcentrated solution range but in other systems produce bizarre conductance maxima.^{26,27} Finally, fairly simple alterations in the structure of the quaternary ammonium cation alter the balance between specific and hydrophobic hydration with surprising consequences. We have synthesized a series of R_4N^+ containing heteroatoms in the side chains that includes one salt melting below 100 °C whose melt is miscible in all proportions with water and another whose aqueous solutions unmix at room temperature.²⁸ The present study approaches some of the above outstanding problems via a different series of new salts in which the cationic shape and the distance of the positive charge from the surface are varied substantially and systematically.

Results

Thermal Properties. The results of hot-stage microscopic examination of the salts studied are given in Table I.

Thirteen of the salts in Table I appear to freeze below room temperature. While it is likely that some may prove to be higher melting, once purified by chromatography, we have not yet succeeded in crystallizing any of them. The following salts were investigated less thoroughly but also probably melt near or below room temperature: $Q_{6,5,5,4}Br$, $Q_{10,8,1,1}Br$,

Table I. Transition Temperatures for Q⁺A⁻

Q ⁺ ^a	A ⁻ = Br ⁻		A ⁻ = ClO ₄ ⁻		A ⁻ = BPh ₄ ⁻	
	transition ^b	T, °C	transition ^b	T, °C	transition ^b	T, °C
Q _{5,5,5,5}	F	101.3 ^d	F	117.7 ^d	F	203.3
Q _{6,5,5,4}			F	83.4		
Q _{6,6,4,4}			F	83.0		
Q _{8,4,4,4}			F	67.3		
Q _{8,5,4,3}		L			I → L	109.5
					II → L	100.5
Q _{6,6,6,2}			F	46.5		
Q _{7,7,3,3}		L	F	45-58 ^e	F	138.8
Q _{8,6,3,3}		L		L	F	110.2
Q _{7,7,5,1}		L (A = I)			F	104.0
Q _{8,6,5,1}		L			I → L	91.0
					II → L	82.5
Q _{9,5,5,1}		L (A = I)			I → L	85.0
					II → L	77.5
Q _{9,6,4,1}		L		L	I → L	65.0
					II → L	58.5
Q _{11,3,3,3}	F	67-68 ^e	F	65.5		
Q _{11,4,3,2}		L			F	100.0
Q _{8,8,2,2}			I → L	62		
			II → L	50		
			III → L	44		
Q _{9,8,2,1}		L			I → L	93.0
					II → L	74.0
Q _{13,3,3,1}	F	71-72 (A = I) ^e				
Q _{9,9,1,1}		L (A = I)	F	52-53 ^e	I → L	98.0
					II → L	85.5
Q _{10,8,1,1}		L		L		
Q _{12,6,1,1}					I → L	87.5
					II → L	79.5
Q _{14,2,2,2}	F	170 dec	I → L	152.0		
			II → L	145.0		
			III → II	80		
Q _{16,2,1,1}	F	180 dec	I → L	155		
			III → II	80		
Q _{17,1,1,1}	F	210 dec	I → L	205 dec		
			II → I	119		

^a Q_{2,2,2,2}⁺ = tetraethylammonium ion, Q_{8,8,2,2}⁺ = diethyldi-*n*-octylammonium ion, etc. ^b F, fusion; II → I, solid-solid transition; I → L, fusion of modification I. ^c L, liquid at room temperature. ^d Reference 11. ^e Sample not pure.

Q_{10,8,1,1}ClO₄, Q_{6,6,4,4}Br, Q_{8,5,4,3}ClO₄, Q_{8,6,5,1}ClO₄, and Q_{9,5,5,1}ClO₄.²⁹ Of these twenty salts, all but three involve a cation of point group C₁. Reduction of the cation's symmetry is a relatively unexplored means of lowering the freezing point. If substantiated, these salts markedly expand the available suite of room-temperature liquid salts.^{12,30} The C₂ cations in this group (Q_{9,9,1,1}, Q_{7,7,3,3}, Q_{6,6,4,4}) have a structural peculiarity in common to which we return in a later section.

Polymorphism appears more frequently with the cations of lower symmetry, with those containing an alkyl chain longer than octyl, and with the polyatomic anions. Q_{16,2,1,1}ClO₄ is probably trimorphic. Modification III crystallizes from the melt and invariably transforms to II at 80 °C. I crystallizes from solution. The II prepared on the hot stage via melt → III → II is so transparent and so invisible between crossed polars that the transition to I (equally transparent) cannot be observed optically, and the ultimate fusion is difficult to fix accurately; the observed freezing point is confirmed by the differential thermogram, which also reveals the II → I transition at 86 °C. Q_{14,2,2,2}ClO₄ also appears to be trimorphic. Modification I crystallizes from solution; the cooled melt crystallizes as modification III, which transforms to II on heating to 80 °C or sometimes to I at 65 °C. Q_{8,8,2,2}ClO₄ is also trimorphic. Modification I grows from solution, II from the melt held at 45 °C, and III from the melt below 44 °C. No solid-solid transitions can be observed. Modification I of Q_{8,5,4,3}BPh₄ crystallizes from solution; modification II crystallizes from the melt but reverts to I on long standing at room temperature. The dimorphs of Q_{9,8,2,1}Ph₄B are obtained in the same way as those

Table II. Transition Temperatures, Enthalpies, and Entropies from DSC Data

salt ^a	transition ^a	T, °C	ΔH, kcal mol ⁻¹	ΔS, eu
Q _{5,5,5,5} ClO ₄	II → I	91	8.8	22
	I → liq	118	4.3	12
Q _{6,5,5,4} ClO ₄	F	82.5	6.3	18
Q _{6,6,4,4} ClO ₄	F	82	8.2	23
Q _{8,4,4,4} ClO ₄	F	65	6.9	20
Q _{6,6,6,2} ClO ₄	F	47	4.5	14
Q _{11,3,3,3} ClO ₄	F	62	6.0	18
Q _{8,8,2,2} ClO ₄	I → L	60	12	36
Q _{14,2,2,2} ClO ₄	III → II	65	3.0	7
	I → L	152	12	36
Q _{16,2,1,1} ClO ₄	III → II	79.5	1.3	3
	II → I	86	4.4	12
	I → L	156	4.6	13
Q _{5,5,5,5} BPh ₄	F	203.5	3.9	8
Q _{8,5,4,3} BPh ₄	I → L	108.5	8.9	23
Q _{7,7,3,3} BPh ₄	F	142	10	25
Q _{8,6,3,3} BPh ₄	F	112	8.2	21
Q _{7,7,5,1} BPh ₄	F	105.5	6.3	17
Q _{8,6,5,1} BPh ₄	I → L	92	9.3	25
Q _{9,5,5,1} BPh ₄	I → L	82	7.4	21
Q _{9,6,4,1} BPh ₄	I → L	64	5.0	15
Q _{11,4,3,2} BPh ₄	F	101	9.3	25
Q _{9,8,2,1} BPh ₄	I → L	93	8.7	25
Q _{9,9,1,1} BPh ₄	II → L	83	9.8	27
Q _{12,6,1,1} BPh ₄	II → L	79	6.6	19
Q _{13,3,3,1} I	F	72	9.0	26

^a As in Table I.

Table III. Binary Phase Diagrams for Salt-Salt Systems, C₁, C₂/A, and C/A₁, A₂

salt 1	T _f , °C	salt 2	T _f , °C	ΔN _a	system type ^a	eutectic or solid-soln min melting temp
Q _{6,5,5,4} ClO ₄	84	Q _{5,5,5,5} ClO ₄	118	2	R III	80
Q _{6,6,4,4} ClO ₄	83	Q _{5,5,5,5} ClO ₄	118	4	R III	80
Q _{8,4,4,4} ClO ₄	67	Q _{6,5,5,4} ClO ₄	84	4	E	45
Q _{8,4,4,4} ClO ₄	67	Q _{5,5,5,5} ClO ₄	118	6	E	56
Q _{6,6,6,2} ClO ₄	47	Q _{5,5,5,5} ClO ₄	118	6	E	60
Q _{11,3,3,3} ClO ₄	66	Q _{5,5,5,5} ClO ₄	118	12	E	60.5
Q _{8,8,2,2} ClO ₄	62	Q _{5,5,5,5} ClO ₄	118	12	E ^b	59
Q _{14,2,2,2} ClO ₄	152	Q _{5,5,5,5} ClO ₄	118	18	E	90
Q _{7,7,3,3} BPh ₄	139	Q _{5,5,5,5} BPh ₄	205	8	R III	129
Q _{8,6,3,3} BPh ₄	110	Q _{5,5,5,5} BPh ₄	205	8	R III	97
Q _{9,6,4,1} BPh ₄	65	Q _{5,5,5,5} BPh ₄	205	10	E	55
Q _{11,4,3,2} BPh ₄	100	Q _{5,5,5,5} BPh ₄	205	12	E	94
Q _{5,5,5,5} BPh ₄	205	Q _{5,5,5,5} ClO ₄	118		R III	114
Q _{5,5,5,5} BPh ₄	205	Q _{5,5,5,5} Br	101		E	96.5

^a E: simple eutectic diagram or Roozeboom type V system (incomplete solid-solid miscibility). R I, R III: Roozeboom type I and type III systems, complete solid-solid miscibility with linear or minimum fp, respectively. ^b Sometimes this system crystallizes in a more complex pattern that appears to involve a molecular compound melting incongruently at 51 °C.

Table IV. Binary Phase Diagrams for Salt-Nonelectrolyte Systems

salt	nonelectrolyte		diagram type ^b	cst ^a
	ethylene glycol	1,2-diphenylethane		
Q _{5,5,5,5} ClO ₄	cst ^a	diagram type ^b		
Q _{5,5,5,5} ClO ₄	100	I		121
Q _{6,5,5,4} ClO ₄	106	I		138
Q _{11,3,3,3} ClO ₄	100	E ^c		128

^a Critical solution temperature, deg. ^b I: no observable freezing-point depression due to poor liquid-liquid solubility at the freezing point. E: eutectic system. ^c Eutectic temperature, 38 °C.

of Q_{8,5,4,3}Ph₄B; fusion of II at 74 °C is followed by recrystallization to I, which then melts at 93 °C.

The differential thermograms generally confirm the hot-stage-microscopic observations and add two additional solid-solid transitions not observed optically.

The rough (±10%) heats and entropies of transition observed by differential scanning calorimetry are shown in Table II.

Solution Properties. The new salts allow us to extend previous observations on the solid- and liquid-phase mutual solubilities of Q⁺A⁻. We had recorded examples in which C₂₄ and C₂₅ quaternary ammonium bromides are miscible in all proportions in the solid phase, but the analogous C₂₄ and C₂₆ bromides showed incomplete miscibility.¹¹ We now hold Q⁺ constant at 20 carbons and measure the distribution of the 20 carbons among the four alkyl groups by an asymmetry number defined as

$$N_a = \sum_{i=1}^4 |5 - n_i| \quad (1)$$

where n_i is the number of carbons in the i th alkyl group. The results in Table III establish that the limit of complete solid-solid miscibility falls at $N_a = 4$ in the perchlorate series and $8 \leq N_a \leq 10$ for the tetraphenylborates. For the one cation where we have both the perchlorate and the tetraphenylborate (Q_{5,5,5,5}) the two salts show complete miscibility in the solid state. Q_{5,5,5,5}ClO₄ and Q_{5,5,5,5}Br were also found to be completely miscible in the solid.¹¹ Despite the fact that the difference in anion size between ClO₄⁻ and Br⁻ is small (radii: Ph₄B⁻, 4.2; ClO₄⁻, 2.0; Br⁻, 1.95 Å),¹⁶ Q_{5,5,5,5}Ph₄B proves to be incompletely miscible with Q_{5,5,5,5}Br.

The results for the salt-nonelectrolyte systems in Table IV show that distortion of the cation shape has little effect on the liquid-liquid miscibility both for a polar and a nonpolar nonelectrolyte, at least up to $N_a = 18$.

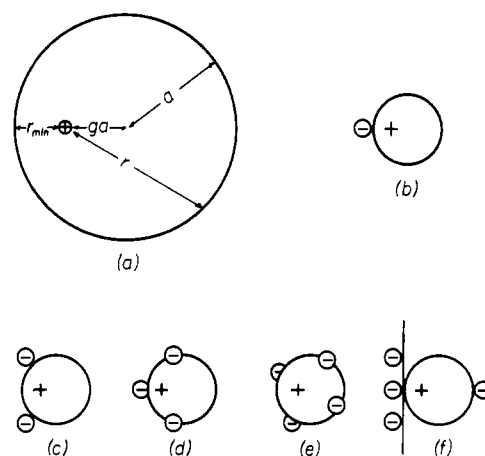


Figure 1. Spherical models of Q⁺ and Q⁺·x A⁻ aggregates. The positive charge lies inside the sphere at a fractional distance g from center to surface.

R_f values for chromatography of the salts on thin silicic acid layers were measured in three solvents; these results are plotted in Figure 6.

Fused-Salt Properties. Densities (d), molar volumes (V_m), and surface tensions (σ) are given in Table V as the least-squares-fitted equations linear in temperature. The only instance of nonlinear temperature dependence of these properties is the surface tension data for Q_{8,8,2,2}ClO₄, which are shown in Figure 4 along with viscosities measured at the same temperatures.

Discussion

Theoretical Models. The structural parameter actually varied in this suite of cations is the distribution of the 20 carbon atoms among the four alkyl chains on nitrogen. This distribution is crudely characterized by the asymmetry number, N_a , from eq 1. N_a varies from 0 for Q_{5,5,5,5}⁺ to 24 for Q_{17,1,1,1}⁺. This set of structural changes alters both the shape of the cation and the asymmetry of charge placement within the cation, and it is not easy to separate these factors. For this purpose we have made use of a combination of crude electrostatic models for the effects of charge asymmetry and empirical models drawn from the behavior of nonelectrolytes to describe the effects of ionic shape. We now describe these models in turn.

The simplest electrostatic model is the sphere with a variably positioned charge shown in Figure 1a. Here a is the radius of

Table V. Liquid Densities, Molar Volumes, and Expansibilities

salt	property	$T, ^\circ\text{C}$	S^b	$10^4 \alpha, ^\circ\text{C}^{-1}$	n^d
$\text{Q}_{5,5,5,5}\text{ClO}_4$	$d = 1.0309 - 0.5887 \times 10^{-3}T$	120-160	0.0022	5.71	12
	$V_m = 382.9 + 0.2616T$		0.93		12
	$\sigma = 34.43 - 0.04636T$		0.03		6
$\text{Q}_{6,5,5,4}\text{ClO}_4$	$d = 1.0116 - 0.4692 \times 10^{-2}T$	85-120	0.0015	4.64	12
	$V_m = 392.3 + 0.2012T$		0.64		12
	$\sigma = 34.94 - 0.06128T$		0.04		4
$\text{Q}_{6,6,4,4}\text{ClO}_4$	$d = 1.0158 - 0.5481 \times 10^{-3}T$	85-120	0.0010	5.40	12
	$V_m = 390.4 + 0.2365T$		0.43		12
	$\sigma = 32.87 - 0.03812T$		0.01		4
$\text{Q}_{8,4,4,4}\text{ClO}_4$	$d = 1.0128 - 0.5540 \times 10^{-3}T$	70-110	0.0014	5.47	12
	$V_m = 392.1 + 0.2359T$		0.66		12
	$\sigma = 34.86 - 0.06576T$		0.02		4
$\text{Q}_{6,6,6,2}\text{ClO}_4$	$d = 1.0143 - 0.5830 \times 10^{-3}T$	60-90	0.0015	5.75	12
	$V_m = 391.5 + 0.2462T$		0.62		12
	$\sigma = 33.24 - 0.05023T$		0.02		4
$\text{Q}_{11,3,3,3}\text{ClO}_4$	$d = 1.0149 - 0.6150 \times 10^{-3}T$	70-100	0.0017	6.06	12
	$V_m = 391.3 + 0.2568T$		0.24		12
	$\sigma = 34.77 - 0.06325T$		0.03		4
$\text{Q}_{8,8,2,2}\text{ClO}_4$	$d = 1.0123 - 0.5776 \times 10^{-3}T$	70-100	0.0023	5.71	8
	$V_m = 392.0 + 0.2481T$		0.98		8
	σ : see Table VII				
$\text{Q}_{14,2,2,2}\text{ClO}_4$	$d = 1.0341 - 0.6840 \times 10^{-3}T$	155-170	0.0009	6.61	12
	$V_m = 379.0 + 0.3209T$		0.42		12
	$\sigma = 32.84 - 0.5620T$		0.02		4
$\text{Q}_{16,2,1,1}\text{ClO}_4$	$d = 1.0154 - 0.6226 \times 10^{-3}T$	155-170	0.0006	6.13	12
	$V_m = 387.1 + 0.2963T$		0.27		12
	$\sigma = 28.31 - 0.04740T$		0.004		4
$\text{Q}_{8,5,4,3}\text{BPh}_4$	$d = 0.9623 - 0.5096 \times 10^{-3}T$	115-145	0.0004	5.29	12
	$V_m = 638.4 + 0.3921T$		0.34		12
	$\sigma = 33.82 - 0.03360T$		0.0077		4
$\text{Q}_{9,9,1,1}\text{BPh}_4$	$d = 0.9496 - 0.4660 \times 10^{-3}T$	110-140	0.0010	4.91	12
	$V_m = 647.7 + 0.3624T$		0.80		12
	$\sigma = 33.33 - 0.03771T$		0.0033		4

^a Temperature range of the measurements. ^b Standard error of estimate of d , V_m , or σ from the equation given. ^c $\alpha = -(dd/dT)/d$. ^d n = number of observations.

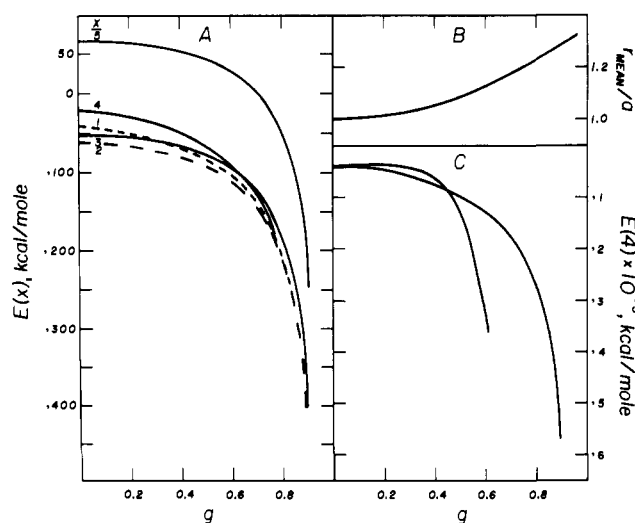


Figure 2. Electrostatic energy and radius as a function of the asymmetry of charge placement. (A) Optimum energy of $\text{Q}^+ + x\text{A}^-$, $x = 1-5$, for Q^+ = sphere of radius 8 Å. (B) Effective electrostatic radius/geometric radius. (C) Optimum energy of $\text{Q}^+ + 4\text{A}^-$ for Q^+ = ellipsoid with $A = 1$ Å, $B = 2$ Å, and $C = 3$ Å: left, \oplus on the x axis; right, \oplus on the z axis.

the sphere, g is the fractional distance of the positive charge from the center of the sphere to the surface, r is the distance of some point on the surface from the positive charge, and r_{min} is the shortest distance from \oplus to the surface, that is, $(1-g)a$. The mean charge-to-surface distance for this model can be calculated as $r_{\text{mean}} = \int r dS / \int dS$. r_{mean} increases with in-

creasingly asymmetric placement of charge (increasing g), and $r_{\text{mean}} > a$ for all $g > 0$ as shown in Figure 2B. However, this does not mean that electrostatic attraction between the cation and nearest-neighbor anions decreases with increasing g , because anions do not sample the surface at random. In fact it is easily seen that the Coulombic attraction felt by a nearest-neighbor anion, or the effective electrostatic radius of the cation, r_e , must depend on the coordination number as well as the value of g . We have computed the optimum configurations and energies of arrays of 1-5 anions about Q^+ as a function of g . The latter are shown in Figure 2A as $E(x)$, where x indicates the number of anions in the aggregate. Thus $E(4)$ is the energy for the $\text{Q}^+ \cdot 4\text{A}^-$ array. Electrostatic attraction increases with increasing g in all cases.

We are particularly interested in the ion pair, $\text{Q}^+ \cdot \text{A}^-$, and the ion aggregates that simulate the coordination number of the fused salt. Since the latter generally decreases somewhat on fusion³⁰ and since crystalline $\text{Q}_{3,3,3,3}\text{Br}$ is tetragonal,²² we expect a coordination number near 4 in the melt. Variation of g alters the $\text{Q}^+ \cdot \text{A}^-$, $\text{A}^- \cdot \text{A}^-$, and $\text{Q}^+ \cdot \text{Q}^+$ electrostatic interactions in the melt or crystal. We assume that nonelectrostatic interactions are independent of g (see below) and that the effect of g on the $\text{Q}^+ \cdot \text{Q}^+$ Coulombic repulsion is negligible in comparison with that on the nearest-neighbor anions. The calculations leading to Figure 2 include explicitly the effects of g on $\text{Q}^+ \cdot \text{A}^-$ attraction and on configuration and electrostatic repulsion of A^- in the nearest-neighbor shell. Consequently this model predicts increasing interionic attraction and increased cohesion in the fused salt as g in the cation is increased.

One simple extension of the above model is substitution of an ellipsoid for the sphere. If the ellipsoid has its center at $(x_0,$

Table VI. Density, Surface Tension, and $\sigma/V_m^{1/3}$ at 110% of the Freezing Point (K) for the Isomeric $Q^+ClO_4^-$

salt	N_a^a	$1/\phi_s^b$	g^c	$d, \text{g cm}^{-3}$	$V_m, \text{mL mol}^{-1}$	$\sigma, \text{dyn cm}^{-1}$	$(\sigma/V_m)^{1/3}, \text{dyn cm}^{-2} \text{mol}^{1/3}$
$Q_{5,5,5,5}ClO_4$	0	1.000	0.000	0.9545	417.0	28.42	3.804
$Q_{6,5,5,4}ClO_4$	2	1.001	0.073	0.9688	410.8	29.35	3.948
$Q_{6,6,4,4}ClO_4$	4	1.013	0.087	0.9658	412.1	29.39	3.950
$Q_{8,4,4,4}ClO_4$	6	1.030	0.117	0.9720	409.5	30.02	4.042
$Q_{6,6,6,2}ClO_4$	6	1.049	0.218	0.9842	404.3	30.64	4.144
$Q_{11,3,3,3}ClO_4$	12	1.111	0.186	0.9709	409.8	30.25	4.073
$Q_{14,2,2,2}ClO_4$	18	1.234	0.234	0.9197	432.7	23.45	3.100
$Q_{16,2,1,1}ClO_4$	22	1.367	0.279	0.9092	437.7	20.23	2.664
$Q_{8,5,4,3}BPh_4$	6	1.034	0.178	0.8870	696.4	28.85	3.255
$Q_{9,9,1,1}BPh_4$	16	1.305	0.348	0.8866	696.7	28.23	3.184

^a Asymmetry number; see text. ^b ϕ_s = shape factor; see text. ^c See Figure 1a.

y_0, z_0), has semiaxes *A*, *B*, and *C*, and has the positive charge at the origin, then *g* is given by

$$g = (x_0^2/A^2 + y_0^2/B^2 + z_0^2/C^2)^{1/2} \quad (2)$$

We have computed the electrostatic energy of geometrically optimized $Q^+ \cdot 4A^-$ arrays for a variety of ellipsoids as a function of *g* (computed via eq 2). These curves are very similar to their spherical analogs, as may be seen for *E*(4) in Figure 2C.

To estimate the effect of cation *shape* on the cohesiveness of the liquid we proceed empirically, using isomeric hydrocarbons as models. In such series the molecular shape affects the packing efficiency, which affects the intermolecular potential and the cohesive energy density.³¹ Typically the cohesive energy density, the surface tension, and the density are strongly correlated.^{31,32} Five different suites of isomers (C_9 and C_{10} alkanes, pentylbenzene isomers, ethylnaphthalene isomers, and isomeric octenes) show the same pattern. As one passes from the most highly branched (most nearly spherical) compounds through progressively more eccentric isomers to the straight-chain compound, the cohesive energy density ($\Delta E_{\text{vap}}/V_m$) falls, passes through a flat minimum, and again rises. This is the characteristic response to changes in molecular shape for liquids whose intermolecular attractive forces are not central, radial ones but are lodged in all the peripheral atoms (London forces).

Parameterization of the Q^+ . To compare results with the models just described, we characterized the Q^+ numerically in the following way. The smallest ellipsoid capable of just containing the cation with all four alkyl chains in their fully extended conformations was found. From the equation of the ellipsoid, *g* was calculated via eq 2 for use as a measure of the charge-placement asymmetry. As a measure of the eccentricity of the ionic shape, we use the engineers' shape factor, ϕ_s , the surface area of a sphere of the same volume divided by the surface area of the minimum ellipsoid. The equations of the minimum ellipsoids and their volumes, eccentricities, and minimum charge-to-surface distances (r_{min}), together with some other computed properties of the extended-chain Q^+ conformers, for all 64 straight-chain isomers of $Q_{5,5,5,5}$ are available as supplementary material (Table S1).

These extended-chain ellipsoids are admittedly extreme models for R_4N^+ ; the real ions, with shapes time-averaged over all conformations of the alkyl groups, are intermediate between these ellipsoids and spheres. We make the assumption, in comparing the *relative* properties of the Q^+A^- salts through the suite of isomeric Q^+ , that the shapes of the real Q^+ are a monotonic function of those of the ellipsoids.

Cohesive Energy Density. The surface tension reflects the magnitude of intermolecular interionic forces in the liquid. We take the quantity $\sigma/V_m^{1/3}$ as a standard measure of the cohesive energy density.^{11,33} Values of *d*, σ , and $\sigma/V_m^{1/3}$ are

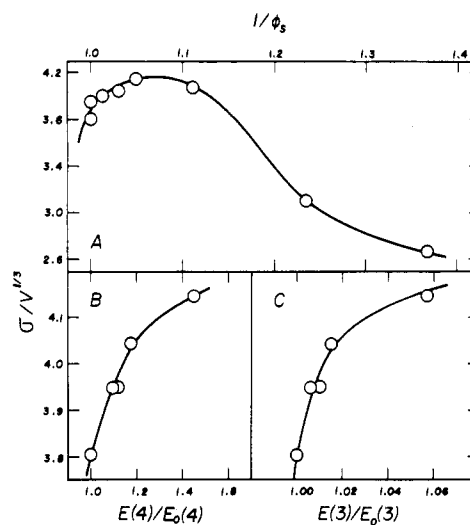


Figure 3. Cohesive energy density vs. (A) surface area of minimum ellipsoid containing Q^+ /surface area of sphere of the same volume and (B) and (C) computed electrostatic energies of the aggregates in Figures 1(e) and 1(d), respectively, expressed relative to the energies at $g = 0$.

compared for the nine $Q^+ClO_4^-$ and two $Q^+BPh_4^-$ salts studied, at the corresponding temperatures $\theta = 1.1T_f$, in Table VI.

The data of Table VI are listed in order of increasing departure from spherical shape (increasing $1/\phi_s$). In this sequence *d*, σ , and $\sigma/V_m^{1/3}$ rise, pass through a maximum, and fall abruptly (Figure 3A). This is precisely opposite the effect of branching in the various hydrocarbon series, and the magnitude of the variability (45%) for the fused salts is considerably greater than for the hydrocarbons (mean, all series, 13%). We conclude that packing factors, if present, are completely overwhelmed by other forces.

The increase in cohesion with increasing *g* predicted by the simple electrostatic models is observed only for the first five $Q^+ClO_4^-$ salts. $\sigma/V_m^{1/3}$ is plotted vs. *E*(3) and *E*(4) in Figures 3B and 3C. (E_0 is the electrostatic energy of the aggregate at $g = 0$.) The 9% increase in cohesion in this series of $Q^+ClO_4^-$ falls between the 6% increase in *E*(3) and the 45% increase in *E*(4) produced by the same excursion of *g* (0–0.218). We see the monotonic rise vs. *E* as a strong indication that alteration of interionic attraction is the controlling interaction mechanism for changes of eccentricity in the low eccentricity range. The agreement of the magnitude of the changes in $\sigma/V_m^{1/3}$ and *E*(3) is fortuitous. *E* does not contain the nonelectrostatic contributions present in the real melt, so that its percentage variation with *g* is inflated. On the other hand, *E* and its dependence on *g* are underestimated because the simple model used ignores penetration of anions between the alkyl chains of

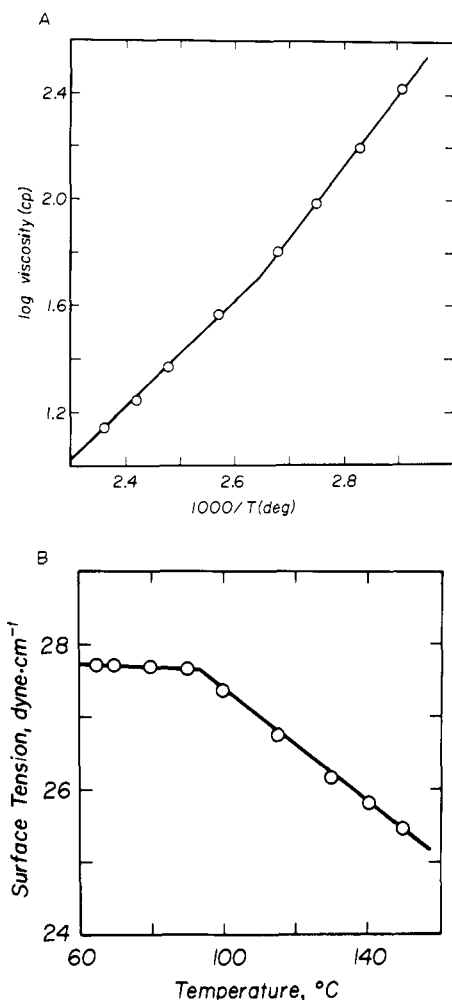


Figure 4. Properties of molten $Q_{8,8,2,2}ClO_4$: (A) $\log \eta$ vs. $1/T$; (B) σ vs. T . Above $95^\circ C$, $\sigma (\pm 0.03) = 31.14 - 0.03811T$ dyn cm^{-1} ; below $95^\circ C$, $\sigma (\pm 0.01) = 27.82 - 0.001966T$ dyn cm^{-1} . Above $110^\circ C$, $\log \eta (\pm 0.009) = -3.697 + 2045/T$; below $110^\circ C$, $\log \eta (\pm 0.009) = -5.330 + 2661/T$ (η in centipoise).

the real Q^+ , which is known for the crystal²² and for ion pairs in solution²³ and is likely in the fused salt.²⁵ Such penetration should become more important as Q^+ becomes more eccentric and some of its alkyl chains become longer and more flexible at their untethered ends.³⁴

The fall of $\sigma/V_m^{1/3}$ above $N_a = 6$ is contrary to expectations based on the electrostatic models. In this range of N_a , approximation of Q^+ as a solid ellipsoid becomes progressively more unrealistic since it ignores the effect of coiling of alkyl chains that are now quite long. Examination of space-filling models shows that when one of the alkyl chains of Q^+ is at least 10 carbons long, conformations exist in which this chain interferes with an anion occupying the most favorable site on the periphery of Q^+ (the spot closest to the positive charge, i.e., at r_{min}). This steric shielding of the front of the cation increases the latter's effective electrostatic radius, and the number of conformations that interfere increases rapidly beyond C_{10} . This phenomenon sets in at the right point to account for the observed maximum in $\sigma/V_m^{1/3}$ vs. N_a or ϕ_s , but we doubt that it is sufficient by itself to account for the rather large drop in $\sigma/V_m^{1/3}$. Since neither cationic shape nor simple electrostatic modeling of Q^+ predicts this decrease in cohesion at large N_a , factors as yet unidentified may be involved. Perhaps, for Q^+ of sufficiently large $1/\phi_s$, the melt begins to modify the alkali-halide structure in the direction of the mesophase structures well-known for long-chain $RCO_2^-Na^+$. The latter involve segregation in different domains of ionic head groups

(plus counterions) and hydrocarbon chains, either as ordered assemblies of long ribbons with head-group cores and hydrocarbon surfaces or as stacked bilayer lamellas.³⁵ We observe no optical anisotropy in any of the molten $Q^+ClO_4^-$ and are not dealing with mesophases, but partial organization along these lines may influence the properties of the isotropic liquid. Crystal structures of the solids and transport properties of the melts would be worthwhile measurements.

Ph_4B^- is larger than ClO_4^- (4.2 vs. 2.3 Å),¹⁶ and much less of its charge is peripheral. Nonelectrostatic interactions should be much more important in the molten $Q^+Ph_4B^-$ than in the $Q^+ClO_4^-$. In fact the cohesions observed for two $Q^+Ph_4B^-$ (Table VI) are nearly identical despite a large difference in eccentricity of Q^+ . With only two $Q^+Ph_4B^-$ measured, we do not yet know if the whole profile of properties vs. g or ϕ_s differs substantially from that of the $Q^+ClO_4^-$.

Prefreezing Phenomena. The temperature dependence of the surface tension of $Q_{8,8,2,2}ClO_4$ is anomalous (Figure 4B). Below ca. $95^\circ C$ σ becomes nearly temperature independent. The intersection of the least-squares lines for the two linear regions falls at $92^\circ C$. Within our experimental error the density is not anomalous. However, the viscosity changes abruptly in this region (Figure 4A). Both temperature regimes give linear $\log \eta$ vs. $1/T$ plots, which intersect at $104^\circ C$. The activation energies for viscous flow, E_η , are 9.4 kcal mol^{-1} above $104^\circ C$ and 12.2 kcal mol^{-1} below $104^\circ C$.

We attribute these observations to a "prefreezing phenomenon" analogous to those observed for some nonelectrolytes.³⁶ If one examines molecular models or the properties of the minimum ellipsoids of the 64 straight-chain isomers of $Q_{5,5,5,5}^+$, $Q_{8,8,2,2}^+$ is set apart from the other $QClO_4$ for which we made measurements by belonging to a small group of ions with two short (1-3 carbons) and two about equally long (7-11 carbons) alkyl chains. This group has the largest values of the smallest radius (9.5-10.4 Å) for rotation of Q^+ (extended conformer) about the best of the seven symmetry axes of the C_4N^+ tetrahedron. In other words these are the ions with the most hindered rotation in the melt. This corresponds precisely to the nonelectrolyte structural types displaying prefreezing phenomena, for instance, *o*-terphenyl vs. the normal *p*-terphenyl.³⁷ Furthermore, the increase in E_η on approaching the freezing point is characteristic.³⁶ The onset of the anomalies for $Q_{8,8,2,2}ClO_4$ at $1.12T_f$ is not unusual, but the abruptness of onset (range $\leq 10^\circ C$) and the linearity of $\log \eta$ in $1/T$ below $1.12T_f$ are. Molten $Q_{8,8,2,2}ClO_4$ shows no optical anisotropy between crossed polars and no change in appearance on the hot-stage microscope near $100^\circ C$.

It would be desirable to check the behavior of other salts of the $Q_{long, long, short, short}$ variety, especially those with the largest values of the best rotational axis. It is interesting in this respect that the maximum value of this radius, 11.4 Å, is computed for $Q_{10,8,1,1}$ which appears to freeze below room temperature. In fact all of the $QClO_4$ with a smallest radius >9 Å melt below about $60^\circ C$, and a rough inverse correlation of T_f with smallest radius holds for all of the perchlorates. Not only do the anomalous nonelectrolytes have lower T_f than their normal isomers but they tend to supercool strongly and often form glasses.³⁶ Our $Q_{8,8,2,2}ClO_4$ does indeed supercool on covered microscope slides by as much as $24^\circ C$ vs. our common observation of $3-8^\circ C$ for the Q^+A^- salts. However, these preparations are not clean enough to make these data quantitatively useful.

Prefreezing of nonelectrolytes is attributed to growth of crystallites possessing structures incompatible with the stable crystalline phase ultimately formed (antycrystalline aggregates).³⁶ These impede viscous flow, diffusion, and crystallization. In the case of $Q_{8,8,2,2}ClO_4$, we see no reason to alter this hypothesis appreciably. We can say that in this case the aggregates are less cohesive than the bulk liquid but are just about as dense.

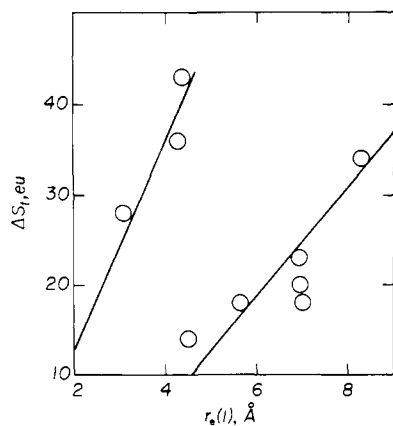


Figure 5. Sum of fusion and solid–solid transition entropies for QClO_4^- vs. the minimum charge-to-surface distances in the ellipsoidal models of the Q^+ .

This appears to be the first clean-cut instance of a prefreezing phenomenon in simple molten salts. Sodium propionate displays a normal temperature dependence of density, viscosity, and conductance down to within 5 °C of T_f .³⁸ (The higher $\text{RCO}_2^- \text{Na}^+$ exist as mesophases above T_f .) There is nevertheless something peculiar about molten $\text{C}_2\text{H}_5\text{CO}_2^- \text{Na}^+$; $E_\eta/RT_f = 8.20$ vs. values in the range 3–4 for alkali halides, nitrates, etc. The corresponding values for the *mesophases* of $n\text{-C}_3\text{H}_7\text{CO}_2^- \text{Na}^+$, etc., are in the range 11–16. For $\text{Q}_{8,8,2,2}\text{ClO}_4^-$ $E_\eta/RT_f = 18.3$ in the prefreezing region and 14 above it. The ratio of the activation energies for viscous flow and conductance is also anomalous in the case of $\text{C}_2\text{H}_5\text{CO}_2^- \text{Na}^+$ and (according to reinterpretation of some data of Walden) in the case of $\text{Q}_{5,5,5,5}\text{SCN}$.²⁵ Conductance and perhaps heat-capacity measurements on $\text{Q}_{8,8,2,2}\text{ClO}_4^-$ may shed some new light on the structural phenomena involved.

Fusion Thermodynamics. There is little variation of ΔH_f or ΔS_f with cation structure among the $\text{Q}^+\text{Ph}_4\text{B}^-$ salts, with the exception of $\text{Q}_{5,5,5,5}^+\text{Ph}_4\text{B}^-$. For this salt ΔS_f amounts to little more than the 5–6 eu produced by translational disordering on breakup of the lattice.^{39,40} This salt is not being disordered in solid–solid transitions above room temperature, according to our thermal observations. A low-temperature study should reveal additional transition(s).

The Q^+ClO_4^- salts show a greater dependence of ΔH_f and ΔS_f on cation structure. The sums of ΔS_f and the solid transition entropies, ΔS_t , decrease with increasing charge asymmetry in Q^+ (Figure 5). When $r_c(1)$ drops below ca. 4.5 Å there is an apparent discontinuity; ΔS_t continues its decline vs. decreasing $r_c(1)$ with a slope similar to that above 4.5 Å, but the values are some 25 eu larger. The break appears at about the same value of N_a at which the cohesive energy density reverses, although the salts used in the two measurements are not quite the same. The approximate linearity observed in Figure 5 does not show up in plots vs. the other parameters measuring Q^+ eccentricity, but in all cases the three most eccentric Q^+ have anomalously high ΔS_f values. The anomaly in ΔS_t could reflect a structural change either in the crystal or in the melt. In the former case a possible explanation is that we are missing a solid–solid transition occurring below room temperature for the less eccentric Q^+ClO_4^- but observing it with $\text{Q}_{14,2,2,2}\text{ClO}_4^-$ and $\text{Q}_{16,2,1,1}\text{ClO}_4^-$. That transition would have to be absent in $\text{Q}_{8,8,2,2}\text{ClO}_4^-$. If the structural anomaly is in the liquid salt, then the anomalous melts must be less structured than those of the less eccentric Q^+ClO_4^- . The cohesive energy densities of these Q^+ClO_4^- salts are indeed unaccountably low (see above), and the combination of low cohesion and low order is a plausible one. It is not, however, the result expected for an alteration in the direction of segregated structures discussed above.

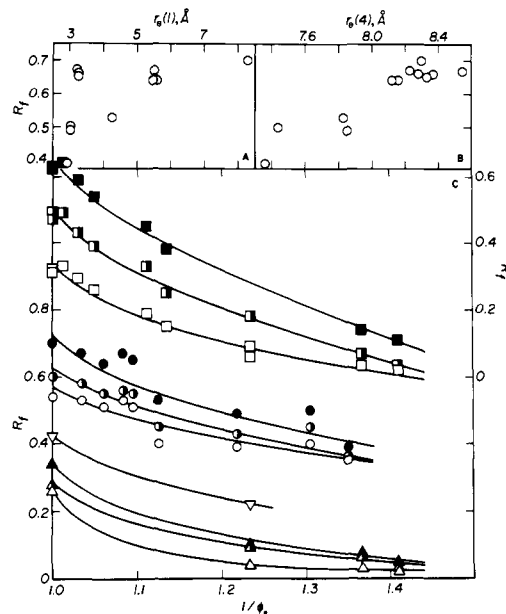
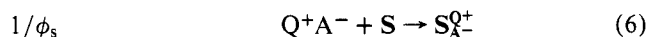
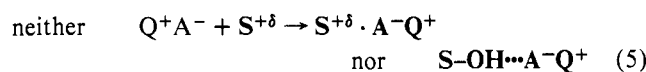
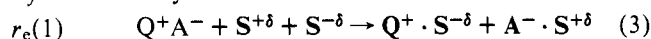


Figure 6. R_f vs. $r_c(1)$, $r_c(4)$, and $1/\phi_s$. \circ , Q^+BPh_4^- ; \square , Q^+ClO_4^- ; ∇ , Q^+I^- ; \triangle , Q^+Br^- . Open symbols, $\text{CHCl}_3\text{-C}_2\text{H}_5\text{OH}$, 95:5; half-open symbols, $\text{CHCl}_3\text{-C}_2\text{H}_5\text{OH}$, 9:1; full symbols, $\text{CCl}_4\text{-C}_2\text{H}_5\text{OH}$, 3:1. All chromatograms on 250- μm layers of silica gel GF.

Thin-Layer Chromatography. The observed R_f values show a strong dependence on the structures of the isomeric C_{20}Q^+ . With a view to identifying the dominant retardation mechanism, we consider the four models represented by eq 3–6. Here S is an active site on the adsorbent; light-face species are in the mobile phase and bold-face species in the stationary phase.

R_f correlated by



Equations 3 and 4 represent association of Q^+ with a polar site on the adsorbent. The former involves electrostatic interactions of the type shown in Figure 1B, whose dependence on charge placement is shown in Figure 2A. In the model of eq 4, Q^+ interacts with A^- and one or more charge sites on the adsorbent; the relevant electrostatic situation (Figure 1F) approximates those in Figure 1C–E, depending on the microscopic structure of the surface. Equation 5 represents interaction of Q^+A^- with the adsorbent mainly through A^- . Equation 6 represents nonelectrostatic interaction of Q^+A^- with the surface, in which case increasing surface area should increase the van der Waals contacts of Q^+ with the surface and increase retardation. The surface area of the ellipsoidal Q^+ relative to that of quasi-spherical $\text{Q}_{5,5,5,5}^+$, A/A_{sph} , is just the reciprocal of the shape factor ϕ_s .

The measured R_f values are plotted in Figure 6. The plots vs. $r_c(1)$ (illustrated by $\text{Q}^+\text{Ph}_4\text{B}^-$ in solvent 1) are widely scattered. The R_f vs. $r_c(4)$ plot (Figure 6B) is better. The reciprocal shape factor proves to correlate the R_f data best (Figure 6C). We take this as an indication that the most important interactions of Q^+ on the adsorbent are nonelectrostatic. The smaller, better H-bonding anions promote retardation, implying some contribution from the interactions of eq 5.

Effective Electrostatic Radii for the Q^+ . The radius of $(\text{CH}_3)_4\text{N}^+$ has been estimated at 2.5,⁴¹ 3.0,¹⁶ and 3.5 Å,²¹ in

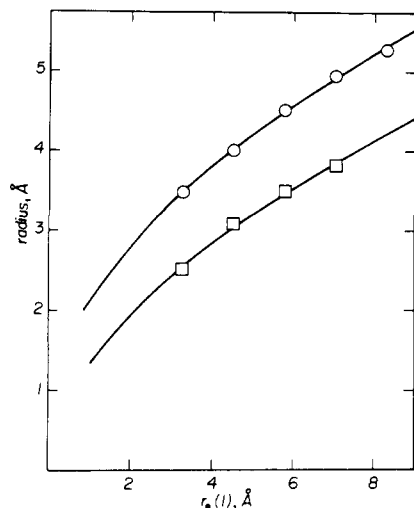


Figure 7. Robinson-Stokes (O) and Masterton (□) radii for the symmetrical Q^+ ($Q^+_{1,1,1,1}$ to $Q^+_{5,5,5,5}$) vs. radii of the minimum sphere containing the fully extended conformation of Q^+ ; $r_e = 0.2303r_{RS} + 0.4153r_M^2 - 0.2486r_{RS} + 0.3421r_{RS}^2$.

various contexts the radius of $(C_3H_7)_4N^+$ appears as 3.0–4.5 Å.⁴¹ This variability in part represents ignorance and in part real differences governed by variable accessibility of the buried change to counterion or solvent. If R_4N^+ is no longer symmetrical, this ambiguity is compounded by the dependence of r_e on g and coordination number discussed above. These unsymmetrically substituted R_4N^+ are now in more frequent use, for instance, in ion-selective electrodes and phase-transfer and micellar catalysis. Consequently it would be useful to have a means of estimating the radius of $R^1R^2R^3R^4N^+$ for any choice of R^1 , R^2 , etc., in such a way that the estimated value is consistent with one of the sets of estimates in common use for the symmetrical R_4N^+ . We have developed means of doing this for two different types of effective radii: first the minimum electrostatic radius, $r_e(1)$, appropriate for interaction of R_4N^+ with a single counterion (Figure 1B), and then the radius of the sphere of the same volume, r_{sph} .

The smallest ellipsoids just containing the extended conformers of the 64 straight-chain isomers of $Q_{5,5,5,5}^+$ and those of the symmetrical R_4N^+ , $n = CH_3$ to $n-C_6H_{13}$, were found as described in preceding sections. The shortest surface-nitrogen distance was determined for each. These distances are given to ± 0.1 Å by equations of the type $d = an_1 + bn_2$, where n_1 and n_2 are the number of carbon atoms in the shortest and second-shortest of the four alkyl groups. These distances derived for a single, extreme conformation were assumed to be a monotonic function of the corresponding "real" values, time-averaged over all conformations. They should be larger than the real values by degrees that increase with increasing length of R . Comparison of these values with the two scales of Q^+ radii in common use is made for the symmetrical Q^+ in Figure 7. The two common scales are sphere-of-equivalent-volume radii determined from molecular models by Robinson and Stokes²¹ and those calculated from nonelectrolyte salting coefficients via scaled-particle theory by Masterton and co-workers.⁴¹ The curves have the expected shape; least-squares equations are given in the figure caption. We now use these equations to scale our minimum radii, $r_e(1)$, from the extended-conformation ellipsoids to the Robinson-Stokes [$r_{RS}r_e(1)$] or Masterton [$r_Mr_e(1)$] scales. Combination of the two operations allows estimation of $r_{RS}r_e(1)$ and $r_Mr_e(1)$ for any Q^+ from n_1 and n_2 . This is conveniently reduced to the nomograph shown in Figure 8. A straight line connecting the number of carbons in the shortest alkyl group (on the left-hand scale) with the number of carbons in the second-shortest alkyl

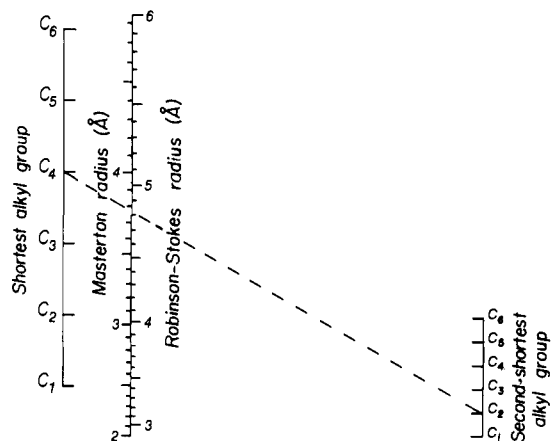


Figure 8. Nomograph for estimating Masterton or Robinson-Stokes radii of unsymmetrical Q^+ .

group (on the right-hand scale) cuts the center scale in the effective electrostatic radii consistent with other values on the RS and M scales. For example, the shortest N^+ -to-surface distance for dimethyldioctylammonium cation, $Q_{8,8,2,2}^+$, is estimated, using the dotted line in Figure 8, as 2.9 Å on the Masterton scale and 3.9 Å on the Robinson-Stokes scale.

To estimate equivalent-sphere radii for unsymmetrical Q^+ , one can take advantage of well-substantiated volume—molecular weight relationships.^{42,43} The plots of $r_{RS}r_{sph}$ and r_Mr_{sph} vs. molecular weight, M , are smooth curves for the symmetrical Q^+ ; the least-squares quadratic equations are given as eq 8a and 8b. The corresponding relationships using the total number of carbon atoms, n_t , in Q^+ as abscissa are equally precise and simpler to use (eq 7a and 7b). As an example, the equivalent-sphere radius of $Q_{8,8,2,2}^+$ ($n_t = 20$) is estimated from eq 7 as 4.0 Å on the Masterton scale and 5.3 Å on the Robinson-Stokes scale.

$$r_Mr_{sph} = 1.83 + 0.1859n_t - 0.00391n_t^2 \quad (7a)$$

$$r_{RS}r_{sph} = 2.83 + 0.1671n_t - 0.00223n_t^2 \quad (7b)$$

$$r_Mr_{sph} = 1.59 + 0.01399M - 0.0000199M^2 \quad (8a)$$

$$r_{RS}r_{sph} = 2.61 + 0.01234M - 0.0000114M^2 \quad (8b)$$

Experimental Section

Tertiary Amines. The compounds prepared are listed in supplementary Table S2. A typical procedure is described for di-*n*-propyl-*n*-tridecylamine.

Di-*n*-propyl-*n*-tridecylamine. 1-Bromotridecane (15.8 g, 0.060 mol, Eastman Kodak White Label) was added slowly to a magnetically stirred solution of di-*n*-propylamine (15.2 g, 0.15 mol) in 20 mL of acetonitrile. Stirring was continued at room temperature for 6 days. The precipitated amine hydrobromide was filtered off, and the filtrate was concentrated at 15 torr and 40 °C, poured into water, and extracted with methylene chloride. The organic phase was extracted with dilute hydrochloric acid, and the extract was basified with 10% sodium hydroxide and extracted with methylene chloride. The combined extracts were dried over anhydrous potassium carbonate and evaporated at 20 torr and 40 °C. The residue was fractionated using a 64 × 1.5 cm glass helices packed column fitted with partial-reflux head. A center cut with constant boiling point and n_D was collected at 164–165 °C (4 torr); 10.2 g (0.036 mol, 60%), n_D^{22} 1.4441.

Quaternary Ammonium Halides. The compounds prepared are listed in supplementary Table S3. A typical preparation is described below.

Triethyl-*n*-tetradecylammonium Bromide. A mixture of triethylamine (4.5 g, 0.044 mol, Eastman Kodak White Label), 1-bromotetradecane (14.4 g, 0.052 mol, Aldrich Chemical Co.), and 20 mL of acetonitrile was refluxed for 6 days. The solvent was removed at 50

°C and 20 torr, and the solid residue was washed with petroleum ether and dried at 50 °C and 20 torr. A hot solution of the resulting solid in ethyl acetate was treated with decolorizing carbon, filtered, and treated with petroleum ether to just short of turbidity. The crystals deposited on cooling (10.6 g) were augmented by a second crop bringing the total to 12.6 g (0.03 mol, 68%) of triethyl-*n*-tetradecylammonium bromide, mp 172 °C (dec). The analytical sample was recrystallized twice from ethyl acetate and dried for 2 h at 22 torr and 40 °C.

Quaternary Ammonium Perchlorates. The compounds prepared are listed in supplementary Table S4. A typical preparation is described below.

***n*-Butyl-di-*n*-pentyl-*n*-hexylammonium Perchlorate.** A mixture of 4.8 g (0.020 mol) of *n*-hexyl-di-*n*-pentylamine, 3.04 g (0.022 mol) of 1-bromobutane (Matheson Coleman and Bell), and 25 mL of acetonitrile was refluxed for 6 days. The solvent was removed at 40 °C and 20 torr, and the residual oil was dissolved in the minimum amount of ethanol and treated with 2.5 mL of 70% perchloric acid in 5 mL of water and 25 mL of 95% ethanol. After 2 h, water was added to turbidity and the solution was cooled to 0 °C. The resulting crystals were filtered, washed with water, dissolved in warm ethanol, and treated with 2 mL of 70% perchloric acid. Addition of 100 mL of water and cooling to 0 °C produced white flakes that were recrystallized twice from aqueous ethanol to give 4.9 g (0.012 mol, 68%) of *n*-butyl-di-*n*-pentyl-*n*-hexylammonium perchlorate, mp 83–83.5 °C.

Quaternary Ammonium Tetraphenylborates. The compounds prepared are described in supplementary Table S5. A typical preparation is given below.

***n*-Butyl-*n*-octyl-*n*-pentyl-*n*-propylammonium Tetraphenylborate.** A solution of 4.95 g (0.013 mol) of crude, oily quaternary bromide (from 1-bromopentane and *n*-butyl-*n*-octyl-*n*-propylamine) in 100 mL of methanol plus 40 mL of water was added to 4.85 g (0.014 mol) of sodium tetraphenylborate in 40 mL of water. After the solution was stirred at room temperature for 6 h, the white precipitate was filtered, water-washed, dried, and recrystallized three times from methanol to give 5.5 g (0.089 mol, 68.5%) of fine needles of *n*-butyl-*n*-octyl-*n*-pentyl-*n*-propylammonium tetraphenylborate, mp 108–109 °C.

Hot-Stage Microscopy. Freezing points, solid–liquid transition temperatures, and critical solution temperatures were observed on a Reichert-Kofler RCH 4065 hot-stage microscope, as previously described.¹¹ Phase diagrams were studied by the contact method⁴⁴ on the same hot stage. Comparison of transition temperatures measured using this apparatus¹¹ with those from adiabatic calorimetry on the same samples⁴⁰ shows that the former are accurate to only ±1 °C though they are reproducible to ±0.2 °C (freezing points) or ±0.5 °C (eutectic temperatures).

Thin-Layer Chromatography. Glass plates bearing a 250-μm layer of silica gel GF (Analtech, Inc.) were dried for 1 h at 130 °C and spotted while warm with 3 μL of acetone solutions (10 mg/mL) of the salts. Developing solvents are identified with the data. Spots were visualized by exposure to iodine vapor.

Differential Thermal Analysis. Samples (0.5–5 mg) were weighed into aluminum disk cells on a Cahn M-10 microbalance. The reference sample was an empty aluminum disk. Differential thermograms were recorded at a heating rate of 2 °C/min using a du Pont 900 differential thermal analyzer.

Density Measurements. The dilatometer was a simple 2 mm i.d. precision bore (Ace Glass Co.) capillary designed more for surveying a large number of compounds and using small samples than for great accuracy. Precision of d for the entire suite of measurements is ±0.001 g/mL. The constant-temperature bath was a cylindrical (diameter 28 cm, height 33 cm) air bath fitted with Pyrex windows, a 1/3 HP, 1700 rpm, 6-in. diameter squirrel-cage impeller, and a thermistor/controller (Yellow Springs Instruments 63-RB). The ASTM 35-C thermometer was calibrated against a Leeds and Northrup, Type 8163 S/N 1758442, platinum resistance thermometer. The spatial thermal homogeneity of the bath, as mapped by its designer, was ±0.1.⁴⁵ Approximately 100-mg samples were weighed into the dilatometer, which was then evacuated to ca. 0.1 torr before fusion of the sample. The vertical height of the meniscus, relative to a reference mark, was measured by means of a Wild KM 801 cathetometer with an 800-mm scale and two telescopes (Wild-Heerbrugg, Heerbrugg, Switzerland). All cathetometer readings and dilatometer fillings were carried out in triplicate.

Surface Tension Measurements. The Pyrex capillary tensiometer is shown in Figure 9. This design is a compromise that allows mea-

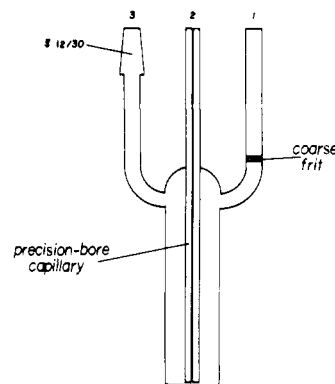


Figure 9. Capillary tensiometer; for dimensions, see Experimental Section.

surements on small amounts of material at the expense of some accuracy as a result of the modest diameter of the outer tube (23 mm i.d.), in which capillarity is not entirely negligible. The potential error in h , the experimental capillary rise, from this source is ca. 2%. This is partly compensated, however, by calibration with standard liquids. The instrument was fabricated from 1.016 mm i.d. precision-bore capillary tubing (Labglass Inc.). A 1–2.5-g sample was placed in neck 1, and neck 3 was attached to the vacuum line. The sample was fused (if solid) in the air bath and filtered through the glass frit into the outer tube by closing neck 2 with a serum cap and opening the stopcock to the vacuum line. After return to ambient pressure and 2-h thermal equilibration (20 min at each succeeding new temperature), the vertical distance between the menisci in inner and outer tubes was measured with the Wild cathetometer.

The tensiometer was calibrated by measurements on water (35 °C),⁴⁶ benzene (30 °C),⁴⁶ and acetanilide (120, 130, 145, 160 °C)⁴⁷ using eq 9. Here r is the capillary radius (cm), σ the surface tension

$$h = 2\sigma/dg \quad (9)$$

(dyn/cm), d the density (g/cm³), g the acceleration due to gravity (980.66 cm/s²), and h the capillary rise (cm). Using the cited sources for the standards, the respective values of r computed were 0.05334, 0.05320, 0.05266, 0.05308, 0.05281, and 0.05283 cm. No systematic temperature dependence is apparent, and the mean value, 0.05312 ± 0.00026 cm, which is close to the nominal radius (0.051 cm), was used in all measurements of σ . The accuracy-limiting element is probably the measurement of h , uncertain to at most 0.1 mm, or approximately 1% for the salts measured. Thus the estimated accuracy is ≤±1% for the salts measured. The precision (mean standard error of estimate of σ from $\sigma = a + bT$) for measurements on a single salt is ±0.1%; from the calibration data (three liquids, six temperatures) it is ±0.5%.

Viscosity Measurements. The modified Ubbelohde viscometer is described elsewhere.⁴⁸ It requires approximately 1 mL of sample and, used in the bath described, delivers viscosity values in the range of 10–300 cP accurate to approximately ±1% and reproducible to ca. 0.5%.

Supplementary Material Available: Table S1 (ellipsoidal representations of quaternary ammonium cations), Table S2 (tertiary amines prepared), Tables S3–S5 (quaternary ammonium salts prepared) (5 pages). Ordering information is given on any current masthead page.

References and Notes

- (1) C. A. Kraus, *J. Phys. Chem.*, **60**, 129 (1956).
- (2) D. F. Evans, C. Zawoyski, and R. L. Kay, *J. Phys. Chem.*, **69**, 3878 (1965).
- (3) C. V. Krishnan and H. L. Friedman, *J. Phys. Chem.*, **73**, 3934 (1969).
- (4) E. M. Arnett, B. Chawla, and N. J. Hornung, *J. Solution Chem.*, **6**, 781 (1977).
- (5) D. F. Evans, J. A. Nadas, and M. A. Matesich, *J. Phys. Chem.*, **75**, 1708 (1971).
- (6) M. R. Kershaw and J. E. Prue, *Trans. Faraday Soc.*, **63**, 1198 (1967).
- (7) J. E. Gordon, "The Organic Chemistry of Electrolyte Solutions", Wiley, New York, N.Y., 1975, Chapter 1.
- (8) H. S. Frank and W.-Y. Wen, *Discuss. Faraday Soc.*, **24**, 133 (1957).
- (9) H. G. Hertz, *Angew. Chem., Int. Ed. Engl.*, **9**, 124 (1970).
- (10) C. Tanford, "The Hydrophobic Effect", Wiley, New York, N.Y., 1973.

- (11) J. E. Gordon, *J. Am. Chem. Soc.*, **87**, 4347 (1965).
 (12) W. T. Ford, R. J. Hauri, and S. G. Smith, *J. Am. Chem. Soc.*, **96**, 4316 (1974).
 (13) Reference 7, Section 3.VIII.
 (14) A. Brändström, "Preparative Ion-Pair Extraction", Hässle, Läkemedel, 1974.
 (15) C. M. Starks, *J. Am. Chem. Soc.*, **93**, 195 (1971).
 (16) E. Grunwald, G. Baughman, and G. Kohnstam, *J. Am. Chem. Soc.*, **82**, 5801 (1960).
 (17) C. V. Krishnan and H. L. Friedman, *J. Phys. Chem.*, **75**, 3606 (1971).
 (18) C. Jolicoeur and H. L. Friedman, *J. Phys. Chem.*, **75**, 165 (1971).
 (19) D. H. Aue, H. M. Webb and M. T. Bowers, *J. Am. Chem. Soc.*, **98**, 311 (1976).
 (20) R. H. Boyd, *J. Chem. Phys.*, **51**, 1470 (1969); M. F. C. Ladd, *Z. Phys. Chem. (Frankfurt am Main)*, **72**, 91 (1970).
 (21) R. A. Robinson and R. H. Stokes, "Electrolyte Solutions", 2nd ed., Butterworths, London, 1959, p 125.
 (22) A. Zalkin, *Acta Crystallogr.*, **10**, 557 (1957).
 (23) H. K. Bodenseh and J. B. Ramsey, *J. Phys. Chem.*, **69**, 543 (1965).
 (24) Reference 7, pp 395 ff.
 (25) G. J. Janz, R. D. Reeves, and A. T. Ward, *Nature (London)*, **204**, 1188 (1964).
 (26) L. C. Kenausis, E. C. Evers, and C. A. Kraus, *Proc. Natl. Acad. Sci. U.S.A.*, **49**, 141 (1963).
 (27) F. R. Longo *et al.*, *J. Phys. Chem.*, **71**, 2755 (1967); N.-P. Yao and D. N. Bennion, *J. Phys. Chem.*, **75**, 3586 (1971).
 (28) J. E. Gordon and P. Varughese, unpublished work.
 (29) $Q_{1,1,2,2}^+$ = diethyldimethylammonium cation, etc.
 (30) J. E. Gordon In "Techniques and Methods of Organic and Organometallic Chemistry", D. B. Denney, Ed., Marcel Dekker, New York, N.Y., 1969, Chapter 3.
 (31) J. H. Hildebrand and R. L. Scott, "The Solubility of Nonelectrolytes", 3rd ed., Dover, New York, N.Y., 1964, Chapter 4.
 (32) A. Ferguson, *Proc. Phys. Soc., London*, **52**, 759 (1940).
 (33) Reference 31, Chapter 23.
 (34) This increasing penetration can be seen in contact distances deduced from ion association constants in solvents of low dielectric constant. Also the Q^+-X^- distance in the crystal increases much less rapidly than the length of the alkyl chains in the series $Q_{1,1,1,1}^+$, $Q_{2,2,2,2}^+$, $Q_{3,3,3,3}^+$ (ref 7, pp 742, 395 ff, and ref 30).
 (35) V. Luzzati in "Biological Membranes", D. Chapman, Ed., Academic Press, New York, N.Y., 1968, Chapter 3.
 (36) A. R. Ubbelohde, "Melting and Crystal Structure", Oxford University Press, London, 1965, Chapter 12.
 (37) E. McLaughlin and A. R. Ubbelohde, *Trans. Faraday Soc.*, **54**, 1804 (1958).
 (38) J. J. Duruz, H. J. Michels, and A. R. Ubbelohde, *Proc. R. Soc. London, Ser. A*, **322**, 281 (1971).
 (39) T. G. Coker, J. Ambrose, and G. J. Janz, *J. Am. Chem. Soc.*, **92**, 5293 (1970).
 (40) J. T. S. Andrews and J. E. Gordon, *J. Chem. Soc., Faraday Trans. 1*, **69**, 546 (1973).
 (41) W. L. Masterton, D. Bolocofsky, and T. P. Lee, *J. Phys. Chem.*, **75**, 2809 (1971).
 (42) B. E. Conway, R. E. Verrall, and J. E. Desnoyers, *Trans. Faraday Soc.*, **62**, 2738 (1966).
 (43) B. E. Conway and L. H. Laliberté in "Hydrogen-Bonded Solvent Systems", A. K. Covington and P. Jones, Eds., Taylor and Francis, London, 1968, p 139.
 (44) L. Kofler and A. Kofler, "Thermo-Mikro-Methoden", Universitätsverlag Wagner Ges. M.B.H., Innsbruck, 1954.
 (45) B. P. Semonian, Thesis, Kent State University, 1974.
 (46) "International Critical Tables", E. W. Washburn, Ed., McGraw-Hill, New York, N.Y., 1926.
 (47) W. E. S. Turner and E. W. Merry, *J. Chem. Soc.*, 2069 (1910).
 (48) V. S. K. Chang, Dissertation, Kent State University, 1975.
 (49) E. T. Borrows *et al.*, *J. Chem. Soc.*, 197 (1947).
 (50) C. A. Brown, A. M. Duffield, and C. Djerassi, *Org. Mass Spectrom.*, **2**, 625 (1969).
 (51) R. S. Shelton *et al.*, *J. Am. Chem. Soc.*, **68**, 753 (1946).

Potential Energy Profiles for Unimolecular Reactions of Organic Ions: $C_4H_9O^+$

Richard D. Bowen^{1a,b} and Dudley H. Williams^{*1a}

Contribution from the University Chemical Laboratory, Cambridge, CB2 1EW, United Kingdom. Received June 26, 1978

Abstract: The slow, unimolecular reactions of six isomers of $C_4H_9O^+$ are discussed in terms of the potential energy profiles over which dissociation is considered to occur. Particular attention is given to the detailed mechanism whereby H_2O loss may occur from the isomers considered. Intermediates, in which a carbonium ion is loosely coordinated to an aldehyde or in which an aldehyde and an olefin are coordinated to a common proton, are postulated for the rearrangement or interconversion of isomeric ions. It is shown that for some reactions of several of the isomers, the rate-determining step is isomerization to another structure of $C_4H_9O^+$, the actual dissociation step being relatively fast in these cases. The reaction schemes proposed are based on mechanistic concepts and are consistent with (i) the competition observed between the various decomposition channels, (ii) the results of 2H -labeling studies, (iii) the kinetic energy release which accompanies dissociation, and (iv) approximate measurements of transition-state energies.

Introduction

In earlier work,²⁻⁴ we have shown how the slow, unimolecular reactions of organic ions in the gas phase may be investigated conveniently by generating the ion in question in a conventional double-focusing mass spectrometer and considering the dissociations which occur in metastable transitions. In general, metastable dissociations occur with little excess energy in the transition state.^{5,6} Consequently, the ability of possible decay channels to compete against one another is critically dependent on the activation energies for the processes concerned.⁷ This is elegantly illustrated by the occurrence of isotope effects in the decomposition of suitably labeled ions. These isotope effects span the entire range of those encountered in solution chemistry and in some cases are spectacularly large. For instance, the metastable decompositions of all the various 2H -labeled methanes have been documented,⁸ and, although

calculations indicate that the threshold for loss of $D\cdot$ is only 0.08 eV above that for $H\cdot$, only CD_4^+ is observed to lose $D\cdot$. Other examples of large primary deuterium isotope effects stem from studies of labeled ethane and propane;⁹⁻¹¹ thus, for $CH_3CD_3^+$, the ratio of $H\cdot$ to $D\cdot$ loss is ca. 600:1.⁹

A useful model for understanding the slow reactions of ions is the construction of a potential energy profile over which dissociation is considered to occur. In this approach the relative energies of reactant ions, plausible intermediates, and possible products are combined with the organic chemist's concept of mechanism so as to deduce the energetically most favorable decay route. In advantageous cases, predictions may be made concerning the dissociation of previously uninvestigated ions. These predictions may refer to the observed decomposition channels,¹² the energy needed to cause dissociation,¹³ the kinetic energy released when reaction takes place,¹⁴ the results of labeling studies,³ or a combination of these factors. In view